3
WORM type memory device based on ionic organotin complex using 1,5-diphenyl-3-(2-pyridyl)formazan ligand

Research Article based on this study:

Birara, S., Betal, A., Lama, P., Sahu, S., & Metre, R. K. (2023). WORM type memory device based on ionic organotin complex using 1,5-diphenyl-3-(2-pyridyl)formazan ligand. *Journal of Molecular Structure*, *1287*, 135708.

3.1 Introduction

A world where digital information is growing exponentially makes it imperative and challenging for scientists to find newer ways to store digital information based on new storage methods or new materials, which will prominently boost the computer's ability to perform more complex tasks [Article et al., 2017],[Y. Li et al., 2018]. As a potential candidate for high-performance data storage, resistive random access memory (RRAM) devices with MIM sandwich structure have gained great attention recently, primarily due to their potential for multilevel data storage with low power consumption, mechanical flexibility, good scalability, high storage density, and stacking feasibility facilitated by multiple resistor states [Cheng, Hou, et al., 2017; Cheng, Xia, et al., 2017; Gu et al., 2014]. There have been ample studies on resistive switching random access memory in the past for several kinds of memory characteristics, including write once read many (WORM) [Shringi et al., 2021], static random access memory (SRAM) [C. L. Wong et al., 2020], flash memory [Zhuang et al., 2010], and dynamic random access memory (DRAM) [Ling, Chang, et al., 2006]. Memory devices that undergo a permanent transition in their resistance, High Resistance State (HRS), and Low Resistance State (LRS) upon the application of a certain electric field across the device terminal are known as WORM memories. Whereas memory devices that are able to switch numerous times between HRS (OFF) and LRS(ON) states are referred to as rewritable memories. Write-once-read-many-times (WORM) operation, based on the resistive-switching (RS) phenomenon, is one of the emerging memory technologies useful for permanent data storage applications, such as archival storage of images, a non-editable database, a radio frequency identification (RFID), and electronic voting. As a result of the tremendous utility of resistive-switching memory, various new materials have been developed recently, including fullerene-polyethylene [Chu et al., 2005], amorphous Si [Jafar & Haneman, 1994] [Niu et al., 2016], virus-NPs [Tseng et al., 2006], inorganic metal oxides [Akinaga & Shima, 2010; Arita et al., 2015; Beck et al., 2000; N. Lu et al., 2015; Sawa, 2008; J. J. Yang et al., 2008], nylon-graphene polymers [Kang, 2016], silver-electrolytes [Guo et al., 2007], multi-walled carbon nanotubes [L. Li & Wen, 2016], organometallic complexes [Stoliar et al., 2015a], and metal/NP-polymers [Heremans et al., 2011a; Ma et al., 2002; Ouyang et al., 2004; Tseng et al., 2005; Y. Yang et al., 2006; Zhou et al., 2014].

Coordination compounds are used in a wide range of applications [Al-Doori et al., 2022; Alheety et al., 2023; Al-Jibori, Al-Doori, et al., 2020; Al-Jibori, Salih, et al., 2020; Allawi et al., 2022], but in recent years, they have gained significant attention as memory devices since these complexes are typically reliable molecular materials and are solution processable. As of now, several different coordination complexes have been successfully utilized in resistive memories. Using a ruthenium-coordinated azo-aromatic compound as the active layer of a resistive memory storage device, Goswami et al. designed a resistive memory device [Goswami et al., 2017a]. A cobalt(II) complex was used in a recent study by Barman et al. to design a WORM type storage device [Barman et al., 2021]. Some of the more examples of such applications include the complexes of Rh(III) [Paul et al., 2012a], Fe(II) [Miyamachi et al., 2012], Ag(I) [Mukherjee et al., 2010a], Au(III) [Au et al., 2015; Hong et al., 2016a; Hong & Yam, 2017a], Cu(II) [Choi et al., 2008; Heintz et al., 1999], Ru(II) [Pradhan & Das, 2008], Ir(III)[Goswami et al., 2014a] and Cr(III)[Kandasamy et al., 2018a] metal ions. Although organic compounds and polymers have led to tremendous advances in resistive memory devices [Gu et al., 2013; H. Li et al., 2010; S. J. Liu et al., 2012; Scott & Bozano, 2007], studies using organometallic complexes [Au et al., 2015; Chan et al., 2017a; Choi et al., 2008; Heintz et al., 1999; Hong et al., 2016a; Hong & Yam, 2017a; Leung et al., 2016; Y. Li et al., 2017; Mukherjee et al., 2010a; Pradhan & Das, 2008] as active components have become pervasive in recent years. Electronic storage devices based on novel organometallic complexes have various advantages, such as easy large-scale fabrication, biodegradability, more flexibility, durability, less expensive materials, and high storage density through judicious molecular designs. The family of main group organometallic complexes has lately gained increasing attention for their flexible, functional properties in different areas such as spintronics, magnetism, and optoelectronics [Bilyachenko et al., 2017; Coste et al., 2019; Levitsky et al., 2019]. Our research group recently reported the development of an organotin sulfide cage-based device [Mishra et al., 2020a] exhibiting excellent resistive memory behavior with a high on-off ratio of 10^3 as well as an organostannoxane-based NDR Device [Mishra et al., 2021] designed using the intramolecular coordination approach. As of yet, only non-ionic organotin complexes with diverse applications have been reported in the literature. To the best of our knowledge, no ionic organotin complex has been explored for its materials applications so far. Among the literature precedents, ionic organotin complexes have been synthesized using several ligands such as 2-benzoylpyridine-derived thiosemicarbazones [Pérez-Rebolledo et al., 2006a], thiamine [Casas et al., 1996], N-(4-hydroxybenzalidene)-p-methoxyaniline [Teoh et al., 1992], 8-methoxyquinoline [Ouyang et al., 1998], 6-methylpyridine-2-carboxaldehyde phenylhydrazone [Teo et al., 2000] and 8-methylaminoquinoline [Hazell et al., 1998]. In these complexes, the ability of the cations to interact with their counterpart organotin anions is largely determined by the attraction between the positive and negatively charged ions as well as by the hydrogen bonds present between them. Chandrasekhar and co-workers, in their recent studies, investigated noncovalent interactions within ionic organotin complexes of 3-(N9-adeninyl) propanoic acid and 2-(N9-adeninyl)acetic acid [Kundu et al., 2015]. Formazan ligands have several unique and potentially useful advantages compared to similar nitrogen-based ligands, including their tunable properties via structural modification, highly delocalized π-systems offering rich optoelectronic properties, redox activity, and low-lying frontier orbitals allowing highly reactive species like radicals to be stabilized [de Vries & Otten, 2022; Gurbanov et al., 2022; Mu et al., 2020]. Furthermore, metal complexes of formazan ligands attracted the attention of researchers due to their ligand-based redox reactions, which show applications in various fields such as multifunctional polymers [Dhindsa et al., 2018; Novoa et al., 2016], cell-imaging agents [Barbon et al., 2017a; Maar et al., 2015a], photoluminescent [Chang et al., 2016; Chang & Otten, 2014] and electrochemiluminescence emitters [Hesari et al., 2018; Maar et al., 2019]. Considering that formazan-based materials offer a wide range of structural variations and fine-tuning possibilities, continual efforts have been made to utilize formazan-based materials for their applications in electronic devices [Milocco et al., 2020; Travieso-Puente et al., 2016a].

With our continuous interest in organotin complexes as molecular materials and formazan-based redox-active ligands, we herein demonstrate that WORM-type memory devices could be achieved by sagaciously combining the two systems. Herein, we report the facile synthesis, structure, and application of a new ionic organotin complex (**1**) with a 2-pyridine substituted formazan ligand as an active material for write once read many (WORM) memory devices with a high on-off ratio of 10^4, good reading capability, low switching voltage, and long term data retention.

3.2 Experimental Section

3.2.1 General Considerations.

The experiment was conducted under a nitrogen atmosphere. Diphenyltin dichloride, 96%, was purchased from Sigma-Aldrich. Hydrochloric acid (SQ) and all the solvents used were purchased from Fisher Scientific company and used as received without any further purifications. The formazan ligand was synthesized according to the published procedure [Johnston et al., 2013a]. In Chapter 2, detailed descriptions of the instruments used for various characterizations are provided.

3.2.2 Device Fabrication

A device with a MIM sandwich structure has been fabricated on an Indium Tin-Oxide (ITO) coated glass substrate. The device structure is shown in Figure 3.1. At first, the ITO-coated glass was cut into small size of pieces with a size of 2×2 cm. The substrates were now dipped into soap water for 15 minutes and washed with water. Then, it was cleaned further with well-known methods, typically with methanol, deionized water, acetone, and deionized water with ultrasonication three times one by one for 15 minutes each. The cleaned substrates were kept in an incubator at 60°C for 12 hours for drying.

The pristine molecule complex **1** was taken with a matrix polymer poly (4-vinylpyridine) (PVP) at a weight ratio of 40:60 soluble in ethanol with a density of 20 mg/ml. The mixture solution was ultrasonicated for 2 hours for homogeneous mixing, and a clear solution was formed. The solution was spin-coated on a previously cleaned ITO-coated glass substrate with a rotation speed of 5000 rotations per minute to get a smooth, thin film. The film was dried for 20 minutes on a hot plate at 70°C. The aluminum contacts have been made utilizing a thermal deposition unit at a pressure of 10^{-6} mbar, and further electrical characterizations have been completed.

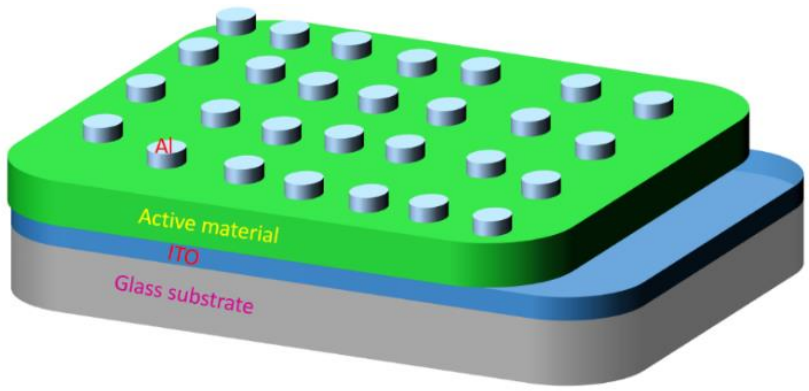


Figure 3.1. The schematic diagram of write once read many (WORM) devices with metal insulator metal (MIM) structure.

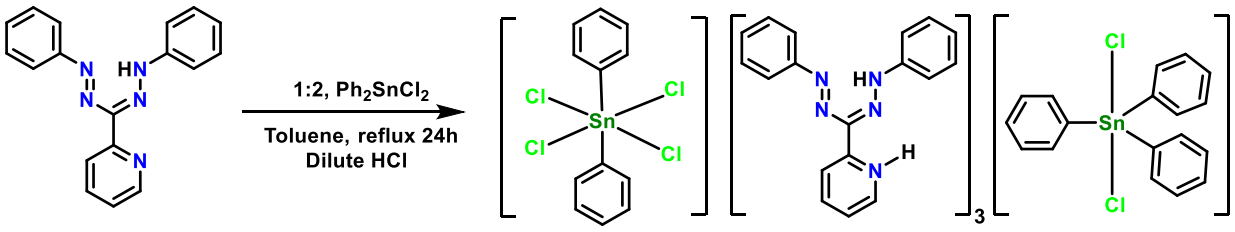
3.2.3 Synthesis

[(Ph_2SnCl_4)$(LH)_3$(Ph_3SnCl_2)]: 1,5-Diphenyl-3-(2-pyridyl)formazan (30.1 mg, 0.1 mmol) was dissolved in 15ml toluene and was stirred for 10 minutes. Diphenyltin dichloride (68.8 mg, 0.2 mmol) was dissolved in 5ml toluene and added to the above solution. 0.1 M dilute hydrochloric acid (4 µL) was added to the reaction mixture, and it was heated under reflux for 24 hours. The solvent was evaporated, and the precipitate obtained was washed with hexane, which on slow evaporation from DCM/Methanol (3:2) solvent mixture, gave single crystals suitable for X-ray diffraction. Anal. Calcd for $C_{84}H_{73}Cl_6N_{15}Sn_2 \cdot 0.75(H_2O)$: C, 57.45; H, 4.28; N, 11.96. Found: C, 56.75; H, 4.754; N, 10.91. ^{1}H NMR (500 MHz, DMSO-d_6) δ 8.77 (d), 8.22 (dd), 7.95 (d), 7.88 (d), 7.69 (dt), 7.52 (t), 7.43 - 7.22 (m) ppm. ^{13}C{^{1}H} NMR (126 MHz, DMSO-d_6): δ 136.8, 135.2, 130.9, 130.7, 129.9, 128.9, 128.3, 128.1, 127.6, 126.8, 124.3, 123.8, 120.5, 119.9 ppm. ^{119}Sn NMR (187 MHz, DMSO-d_6) δ -330.19, -400.93 ppm. FT-IR(KBr): 3586 (m), 3344 (m), 3069 (m), 2675 (m), 1593 (m), 1482 (s), 1429 (m), 1272 (m), 1160 (m), 1062 (w), 740 (s), 682 (s), 564 (w),439 (s) cm^{-1}. UV-Vis(MeCN): λ_{max} (ε, M^{-1} cm^{-1}) 302 (68421), 459 (73853) nm.

3.3 Results and Discussion

3.3.1 Synthetic Aspects

Treatment of 1, 5-Diphenyl-3-(2-pyridyl)formazan with 2 equivalents of Ph_2SnC1_2 in toluene resulted in the formation of an ionic organotin complex [(Ph_2SnCl_4)$(LH)_3$(Ph_3SnCl_2)] (**1**) in good yield (Scheme 3.1). Single-crystal X-ray crystallography was used to determine the molecular structure of **1**. Complex **1** was further successfully characterized by utilizing IR, UV-Vis, ^{1}H, ^{13}C{^{1}H}, and ^{119}Sn NMR spectroscopy. The ^{1}H NMR spectrum of **1** in DMSO-d_6 shows the presence of signals in the range of δ ~7-9 ppm that can be attributed to phenyl substituents on Sn and formazan ligand (Figure 3.2). However, there is no NH proton peak in the ^{1}H NMR spectrum, suggesting that these protons have high mobility in the organic solvent. Furthermore, a doublet signal was seen in the spectrum at δ 8.77, which was attributed to a proton bonded to the carbon next to the pyridine nitrogen, and further doublet of doublet signal around δ 8.22, signals corresponds to three protons of the protonated pyridine ring of the ligand [Johnston et al., 2013b]. The ^{119}Sn NMR spectrum of **1** shows the presence of two signals, appearing at a chemical shift of δ -330 ppm and -400 ppm, indicating the presence of two different chemical environments surrounding the Sn center (Figure 3.2). These different environments are ascribed to two different tin anionic moieties, one that involves the tetrachlorodiphenyltin(IV) anionic moiety where the Sn center possesses a distorted octahedral geometry, and other involving a dichloridotriphenylstannate(IV) anion which adopts a trigonal bipyramidal geometry around the Sn center. Earlier reported ionic organotin complexes containing $Ph_2SnCl_4^{2-}$ anionic moiety have been found to have ^{119}Sn NMR chemical shift ranging from δ -174 to -253.2 ppm [Al-Allaf et al., 2003; García-Seijo et al., 2001; Pérez-Rebolledo et al., 2006b].



Scheme 3.1. (a) Synthesis of the complex **1**.

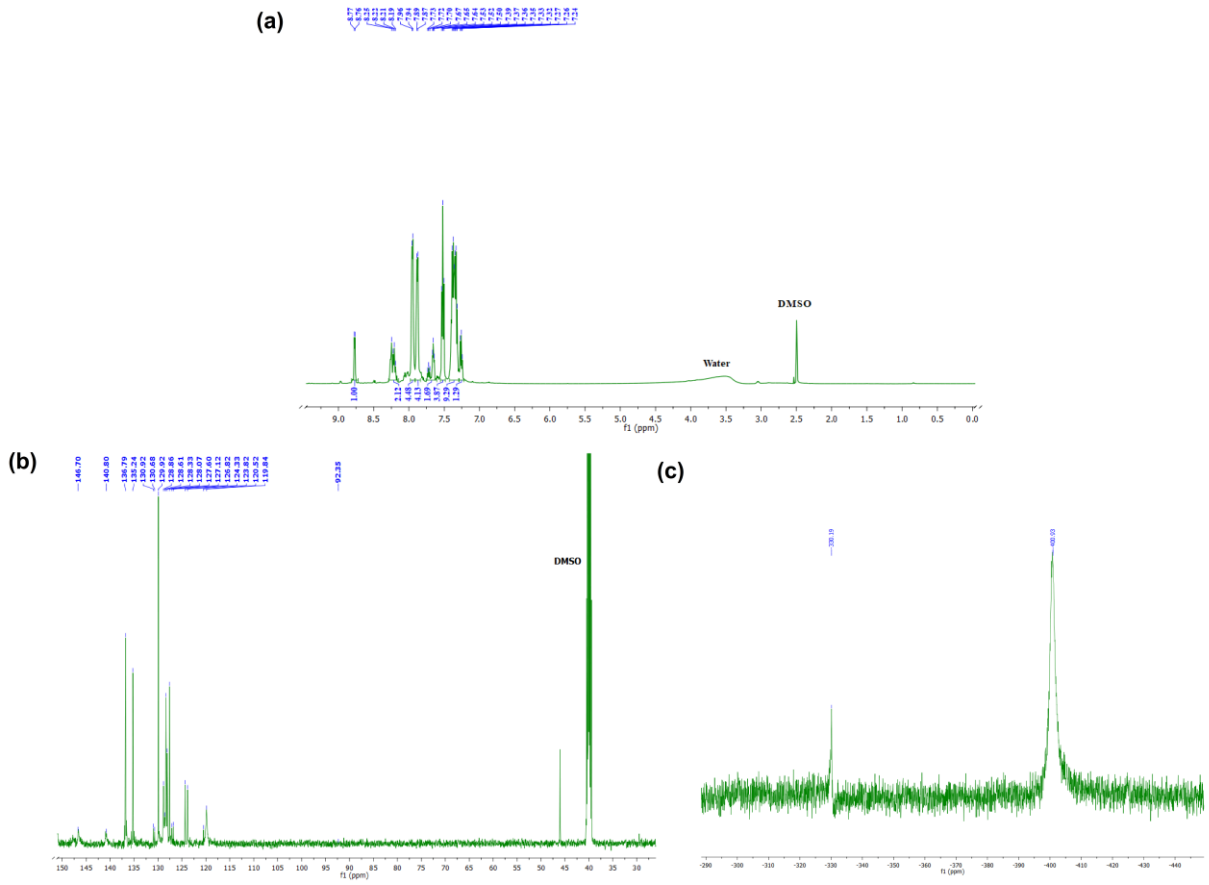


Figure 3.2. (a) ^{1}H NMR, (b) ^{13}C NMR and (c) ^{119}Sn NMR spectrum of complex **1.**

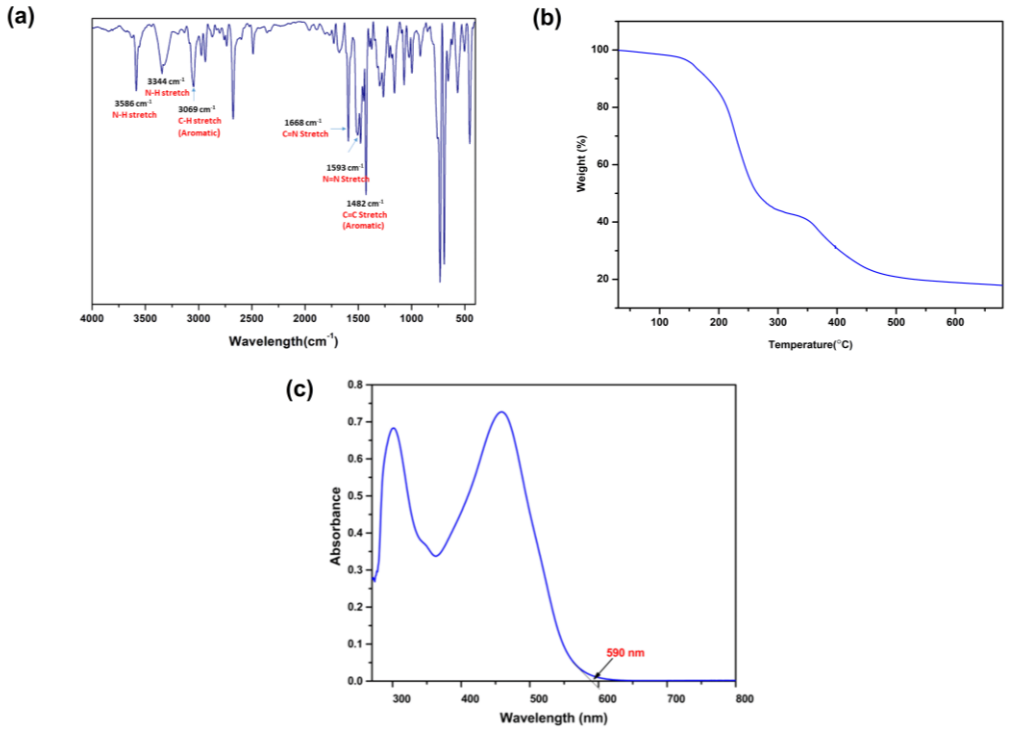


Figure 3.3. (a) IR spectrum, (b) Thermogravimetric analysis (TGA) plot, and (c) UV-Vis absorption spectrum(λ_{onset}= 590 nm) for complex **1.**

The IR spectrum of **1** reveals the presence of a new band at 3586 cm^{-1} ν(N–H), which was absent in the original ligand, indicating the protonation of the ligand [Johnston et al., 2013a] (Figure 3.3). UV-vis absorption spectrum of complex **1** was measured in acetonitrile solution to determine its optical properties. The red solution of complex **1** exhibited two absorption bands, one at 302 nm and another one at 459 nm, corresponding to formazan ligand-centered π→π* transitions primarily involving HOMO and LUMO orbitals (Figure 3.3). According to thermogravimetric analysis (TGA), the complex is thermally stable up to 150°C, and the residual yield at 600 °C was found to be 20% (Figure 3.3).

3.3.2 Single Crystal X-ray Crystallography

The Single crystal X-ray crystallographic analysis of complex **1** was carried out to confirm the solid-state structure of the complex. Complex **1** crystallizes in the monoclinic *C*2/*m* space group and consists of two crystallographically independent Sn(IV) ions in the asymmetric unit (Figure 3.4). In the asymmetric unit, the first Sn(IV) (Sn1) has 0.5 occupancy and is coordinated to two phenyl anions (one has half occupancy, and another has full occupancy) along with one full chloride ion. The second Sn(IV) (Sn2) has 0.2 occupancy and is coordinated to one phenyl anion (half occupancy) along with 0.8 occupancy chloride anion. Together, the Sn(IV) discrete units give rise to a negative charge that is balanced by the protonated nitrogen atom of the pyridine unit of the formazan ligand in the asymmetric unit. In addition, complex **1** consists of disordered 0.25 water molecules in the asymmetric unit, which has been squeezed using the program PLATON [Spek, 2015]. Overall, in the molecular structural formula, the X-ray crystal structure of **1** reveals the presence of two anionic organotin moieties, namely, di-anionic tetrachlorodiphenylstannate(IV) and mono-anionic dichloridotriphenylstannate(IV) and three planar protonated formazan ligand.

In tetrachlorodiphenylstannate(IV) anion $[Ph_2SnCl_4]^{2-}$, tin(IV) ion possesses a distorted octahedral geometry, four chloride occupies the equatorial sites [Sn-Cl distances; 2.581(7) Å], whereas the apical sites are occupied by two phenyl groups [Sn-C distances; 2.113(5) Å]. Bond length values observed in the present instance are in a similar range found for the ionic organotin complex containing bis(8-(methylamino)quinolinium) cation reported in the literature [Hazell et al., 1998]. Consequently, there is an exact 180° angle between the two trans phenyl groups, and the phenyl rings almost lie perpendicular to the equatorial plane of SnCl~4~ [C11—Sn2—Cl2 = 88.46 (11) °, C11—Sn2—$Cl2^{ii}$ = 91.54 (11) °]. On the other hand, the Sn center in dichloridotriphenylstannate(IV) anion $[Ph_3SnCl_2]^-$ possesses a usual trigonal bipyramidal geometry, whereas phenyl groups are arranged equatorially [Sn-C distances 2.154(2) and 2.158(3) Å], and the chlorine atoms [Sn-Cl distances 2.578(7) Å] are present in the axial position.

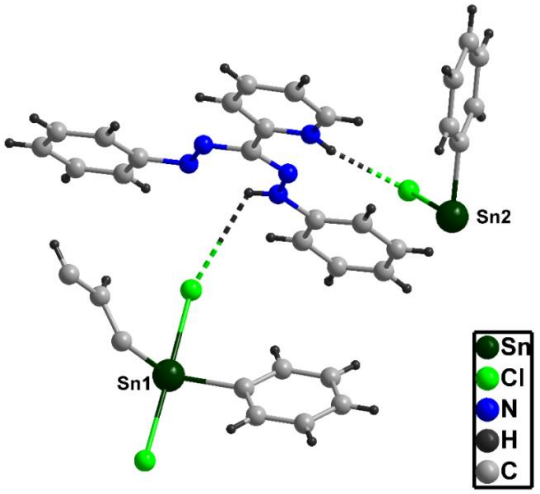


Figure 3.4. The asymmetric unit of complex **1**.

Table 3.1. Crystal data and structure refinement for complex **1** (CCDC 2178294).

Empirical formula	$C_{120}H_{104}N_{20}Sn_{2.8}Cl_{7.2}$
Formula weight	2413.80
Temperature (K)	298(2)
Crystal system **Color, habit**	Monoclinic Dark red, block
Space group	C2/m
a (Å)	14.263(3)
b (Å)	49.490(10)
c (Å)	8.9289(18)
α (°)	90
β (°)	115.935(2)
γ (°)	90
Volume (Å³)	5668(2)
Z	2
ρ_{calc}, g.cm^{-3}	1.414
μ, mm^{-1}	0.841
F(000)	2453.0
Crystal size (mm)³	0.448 × 0.366 × 0.316
Radiation	Mo K_α (λ = 0.71073)
2Θ range (°)	3.28 to 49.994
Index ranges	-16 ≤ h ≤ 16, -58 ≤ k ≤ 58, -10 ≤ l ≤ 10
Reflections collected	54242
Independent reflections	5073 [R_{int} = 0.0328, R_{sigma} = 0.0149]
Data/restraints/parameters	5073/0/353
Goodness-of-fit on F²	1.098
Final R indexes [I>=2σ (I)]	R_1 = 0.0281, wR_2 = 0.0771
Final R indexes [all data]	R_1 = 0.0317, wR_2 = 0.0799
Largest diff. peak/hole (e Å^{-3})	0.57/-0.65

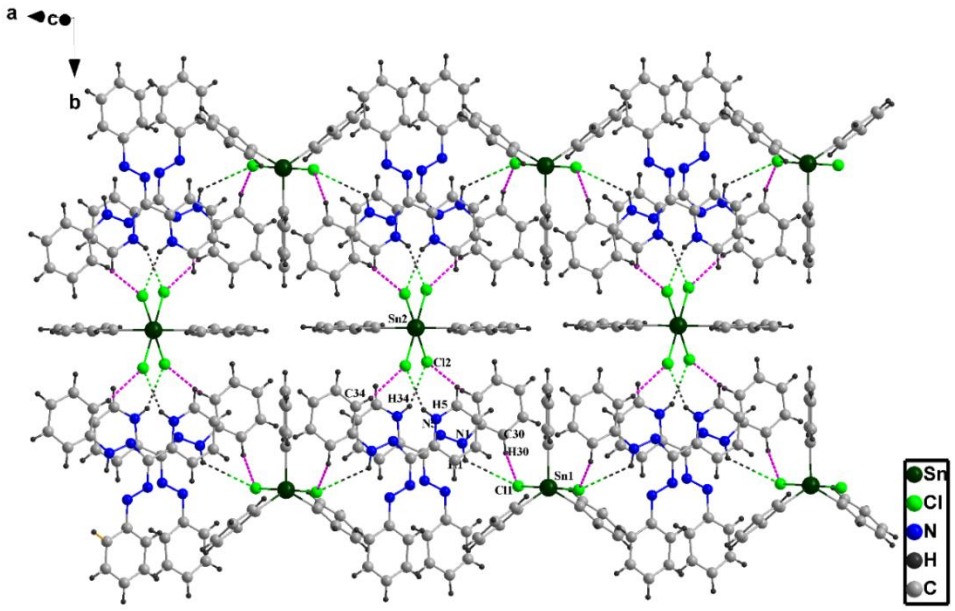


Figure 3.5. N-H--Cl and C-H--Cl interactions in complex **1**. Bond distances (Å): N5H5···Cl2, 2.387; N1H1···Cl1, 3.163; C34-H34···Cl2, 2.764; C30-H30···Cl1, 2.867. Bond angles (deg): N5-H5-Cl2, 142.767; N1-H1-Cl1, 120.103; C34-H34-Cl2, 163.827; C30-H30-Cl1, 120.735.

The formation of hydrogen bonds among N–H···Cl atoms is the most noticeable feature of molecular packing of **1**. Each $[Ph_2SnCl_4]^{2-}$ anion is hydrogen bonded to four nearby protonated formazans, whereas each $[Ph_3SnCl_2]^-$ anion is hydrogen bonded to two nearby protonated formazans through NH···Cl interactions. The protonated site of the cationic ligand is bonded to the $[Ph_2SnCl_4]^{2-}$, with an N5H5···Cl2 distance of about 2.387 Å, and the other N-H proton present in cationic formazan core is hydrogen bonded to $[Ph_3SnCl_2]^-$ with an N1H1···Cl1 distance of about 3.163 Å (Figure 3.5). Additionally, there are C-H···Cl interactions in which the C-H of protonated formazan interacts with the Cl of the organotin moieties. In the case of $[Ph_2SnCl_4]^{2-}$ anion, the C34-H34···Cl2 distance is 2.7643 Å, whereas in the case of $[Ph_3SnCl_2]^-$, C30-H30···Cl1 distance is 2.8676 Å (Figure 3.5). The other dominant supramolecular interaction in the crystal structure of complex **1** is offset π-π stacking of the aromatic rings present in the cationic formazan ligand. The alternating protonated formazan is supported by weak aromatic stacking amongst the offset aromatic entities of the fused cores with ring-centroid distances of 3.889 Å and 3.790 Å (Figure 3.6). The collective result of these multiple secondary interactions culminates in a 3D supramolecular structure. Such supramolecular assemblies are well known for main-group organometallic complexes. The unit cell of complex **1** is displayed in Figure 3.7.

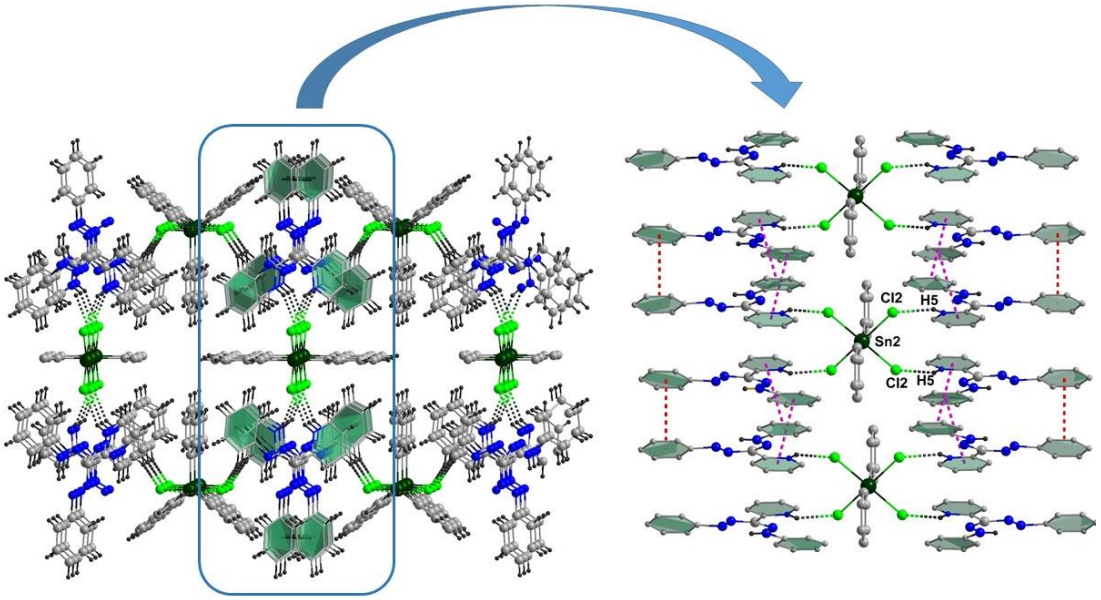


Figure 3.6. Supramolecular assembly for complex **1** involving π – π interactions. Bond distances (Å): 3.889(red dotted line) and 3.790 Å (pink dotted line).

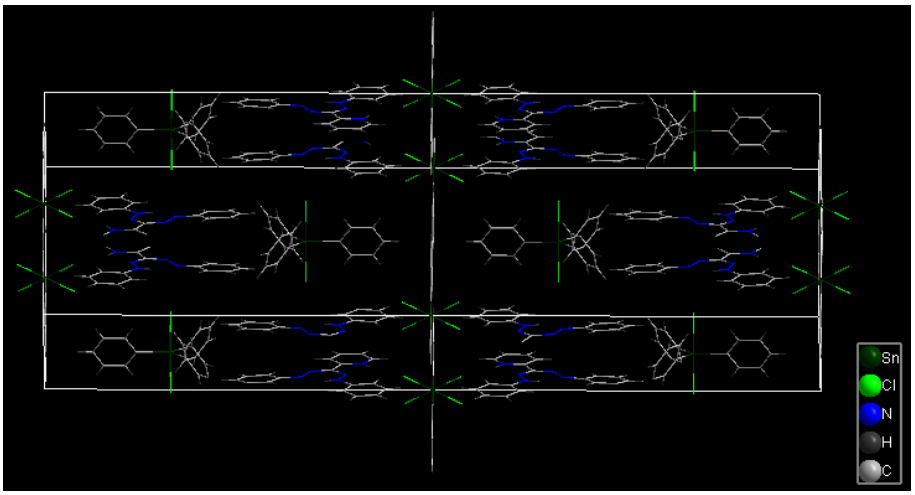


Figure 3.7. Unit cell of complex **1**.

3.3.3 Memory Device Studies

The voltage sweeps were applied from -1.5 V to 1.5 V region; the applied voltage initiates from -1.5 V, increases to 1.5 V, and retraces back to -1.5 V as shown by blue arrows (Figure 3.8 (a)). The current of the device remains at a high resistance state (HRS); that is, the current is low from -1.5 V to 1.03 V and switches to a low resistance state (LRS). The device remains in the same state even after applying a reverse bias voltage of -1.5 V, which means the device acts as a write-once-read-many (WORM) device. Many current-voltage iteration cycles were taken, and it has been noticed that the device remains at LRS after switching from HRS to LRS. The 1st, 5th, 10th, and 20th cycles are shown in Figure 3.8 (a), which shows the WORM properties of the device. The stability of the device has been studied from the retention curve, as shown in Figure 3.8 (b). A retention study is important to know the stability of the device at a particular state (LRS or HRS). Before applying a write pulse, read the current at a voltage of 0.3 V, called read voltage, and the device was at HRS. After applying a write pulse of 1.5 V for 10 seconds, the device switches to LRS. The device stays at the LRS state even after a negative voltage is applied. Figure 3.8(b) shows that the retention study was taken for more than 4500 seconds, and two different resistance states can be found.

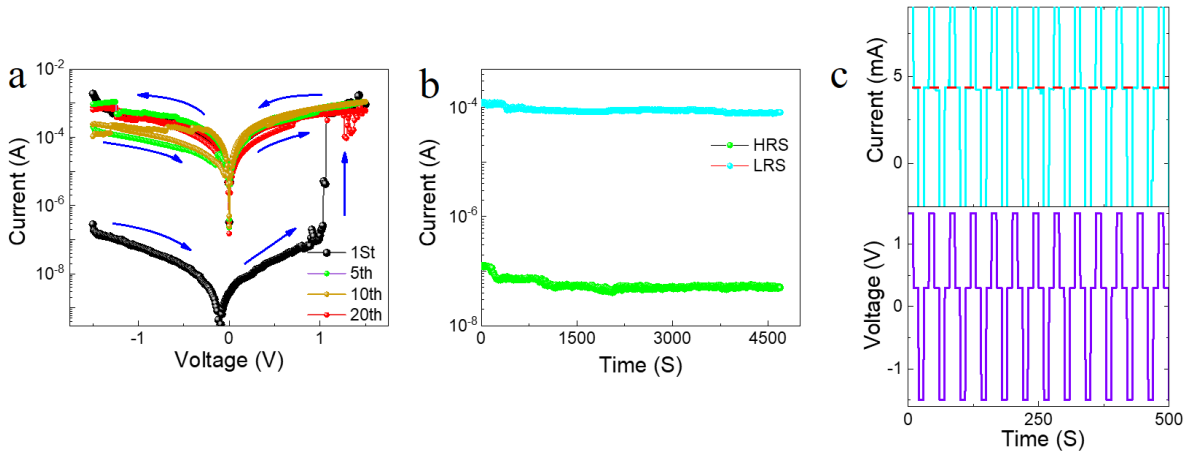


Figure 3.8. (a) Current-voltage iteration of the device for the 1st, 5th, 10th, and 20th cycle. (b) Checking the device stability with time (A particular read voltage was applied to the device before and after write, and the device is showing two resistance states). (c) Random access study after writing the data (The device shows a fixed resistance state after erasing and writing voltage).

The random access study of the device has been performed with a voltage pulse of 1.5 V as write, -1.5 V as erase, and 0.3 V as read voltage, as shown in Figure 3.8 (c). At first, a write pulse was applied for 10 seconds to switch from HRS to LRS and read the state with a read pulse for 10 seconds. It was noticed that the device remains at LRS after writing the pulse. Then, to check if the data was written permanently or not, a reverse voltage pulse (erase pulse) was given for 10 seconds, and read the resistance state again, which showed the same resistance state. This confirms the device as a WORM.

The atomic force microscopy (AFM) study was performed on the thin film of the device using Park System (XE-70) with a non-contacting mode (Figure 3.9). The surface morphology image was taken using an NCST-Au tip with a scan speed of 1 line per second and a cut-off distance of 12 nm. The surface topography of area 10 nm×10 nm is shown in Figure 3.9. The topography shows an average roughness of 13.24 nm and a root mean square roughness of 16.91 nm. The area histogram of the image is shown below, which indicates the Gaussian curve of roughness. The peak of the curve is near 0 nm roughness, which indicates most of the areas are smooth.

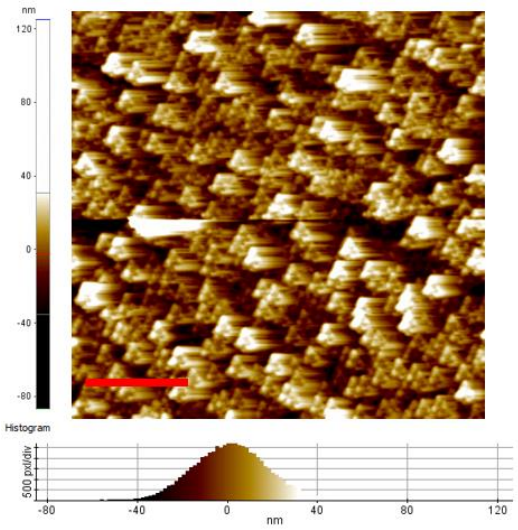


Figure 3.9. Atomic force microscopy of the thin film deposited by spin coating on ITO-coated glass substrate. The area histogram of roughness shows the Gaussian curve of roughness. The red scale bar indicates 2.5 μm on the image.

3.3.4 Electrochemical Properties and Proposed Mechanism.

Redox properties of complex **1** were studied with the help of cyclic voltammetry (CV) using a three-electrode cell system in a DMF solution containing tetrabutylammonium hexafluorophosphate ($TBAPF_6$) as the supporting electrolyte [Figure. 3.10 (a)]. Complex (**1**) shows oxidation as well as reduction features within the accessible electrochemical window. The cyclic voltammogram of complex **1** exhibits two anodic waves at 0.786 V and 1.13 V, which can be attributed to the oxidation and the protonation of the ligand, respectively, present in complex **1**. The observed values in the present instance are in close agreement with those reported in the literature [Synthesis et al., n.d.]. Complex **1** also shows the two reduction peaks at -0.445 V and -0.99 V [Synthesis et al., n.d.]. The onset value corresponding to the first oxidation peak at 0.786 V is found to be 0.61 V. This value corresponds to the HOMO energy level of **1** at -5.08 eV and the LUMO energy level is -2.98, which is estimated from the difference between the HOMO level and optical band gap (Table 3.2). Ferrocene reference energy level is 4.8 eV and $E_{ox.}$ (ferrocene) is the potential when ferrocene starts being oxidized (0.33 eV vs. Ag/AgCl). The energy barrier between the Al electrode and the LUMO energy level of complex **1** is 1.32 eV [Figure 3.10(b)], which is greater in contrast to the energy barrier of ITO and HOMO levels. Thus, in the Al/Complex **1** /ITO device, holes seem to be involved in initiating the conductivity for the electric memory measurements.

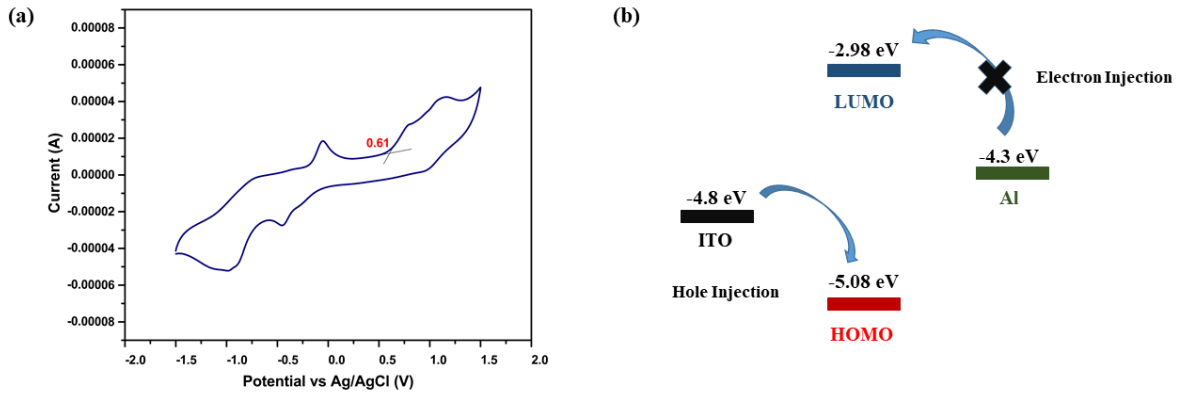


Figure 3.10. (a) Cyclic voltammogram of complex **1** (ca. 1 mM solution of **1** in DMF; scan rate = 0.1 $V \cdot s^{-1}$); 0.1 M $[Bu_4N][PF_6]$ electrolyte. (b) Schematic diagram of the charge injection processes in the memory device.

Table 3.2. Optoelectronic properties of complex **1.**

Compound	$E^{opt}_{HOMO-LUMO}$ (eV)	$E_{ox,\ onset}$ (V)	E_{HOMO} (eV)	E_{LUMO} (eV)
1	2.10	0.61	-5.08	-2.98

$E_{HOMO} = -(E_{ox,onset} + 4.8 - E_{(Fc+/Fc,onset)})$, $E_{(Fc+/Fc,onset)} = 0.33$ V, $E_{LUMO} = E_{HOMO} + E^{opt}_{HOMO-LUMO}$, $E^{opt}_{HOMO-LUMO} = 1240/\lambda_{onset}$ (λ_{onset}= 590 nm).

To get an idea of the charge conduction mechanism, the I-V characteristics curve was plotted on a logarithmic scale, and the data was fitted linearly. The HRS has two different slopes, whereas the LRS has only one slope, as shown in Figure 3.11. At low voltages, the hole injection into the film from the ITO would have enough power to overcome the thermally generated Schottky barrier, indicating the operating memory behavior to be the charge-transport controlled thermionic emission. From 0 V to 0.27 V, the logarithmic current is proportional to the square root of applied voltage, which further indicates the thermionic emission, and it can be expressed by the equation

$$I \propto T^2 exp\left(\frac{-q\left(\emptyset_B - \sqrt{\frac{qV}{4\pi\epsilon}}\right)}{K_B T}\right) \qquad (1)$$

$\emptyset_B$, V, K_B, and T are the barrier height, applied voltage, Boltzmann constant, and absolute temperature. 0.28 V to 1 V, the current varies quadratically with applied voltage suggesting the space charge limited conduction (SCLC) of the charge carrier. After exceeding the turn-on threshold voltages, the current increases sharply to the LRS, where the current changes linearly with voltage (I∝V), which is considered as ohmic conduction and indicates the formation of the metallic filament. As a result, thermionic emission, SCLC, and filament formation contribute to the switching behavior of the studied complex **1** memory device (C. L. Liu et al., 2009).

Amidst various types of memristors, the redox ligands-based memory devices are generally known to operate through the formation and rupture of conductive filaments (CFs) in addition to the redox pathways. The switching mechanism of the device in the present instance can be explained by a well-known electrochemical metallization process [Munjal & Khare, 2019]. For this process, one electrochemically active electrode should be deposited here. Here we have deposited aluminum (Al) as an electrochemically active metal. The schematic of the switching mechanism

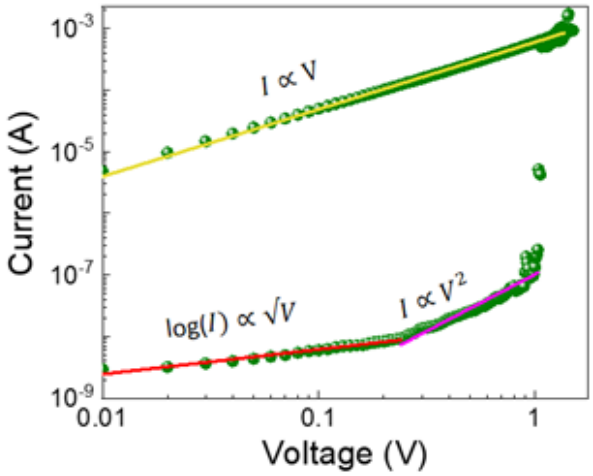


Figure 3.11. The I-V curve plotted in a logarithmic scale to analyze the charge conduction mechanism.

is shown in Figure 3.12. Upon applying a positive bias on Al contact, the Al cations are rippled by electrostatic force and start to move through active material. The Al ions move through the material and start accumulating on the ITO substrate. The ions make a filament-like permanent metal path to flow the current. During metal migration, the device was in HRS, and as soon as the filament formed, the device switched to LRS. As the device forms a permanent filament, the device stays at LRS persistently; hence, WORM behavior can be realized.

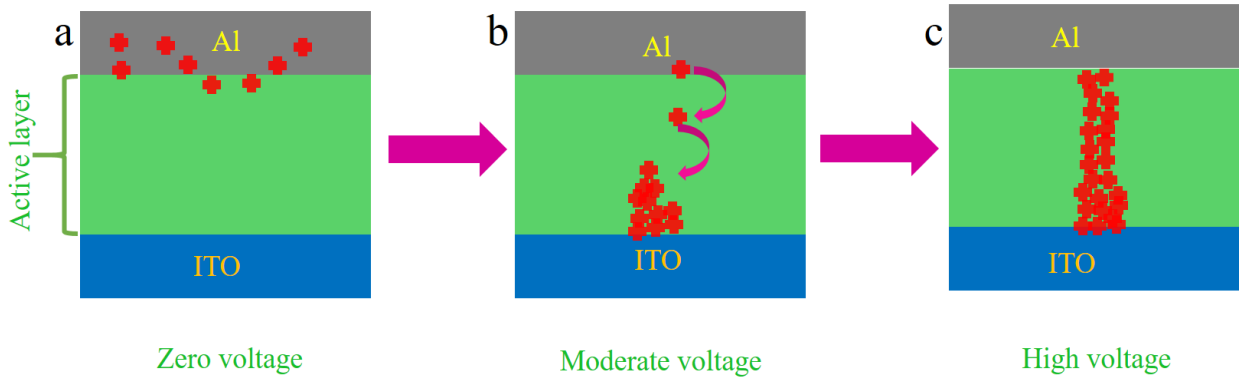


Figure 3.12. The schematic diagram of the switching mechanism of the device. (a) At zero bias voltage, the Al ions are randomly oriented. (b) At moderate voltage, Al ions started accumulating on the ITO surface. (c) At sufficiently high voltage, Al ions formed a permanent metallic path leading the device to LRS.

3.4 Conclusion

In conclusion, an ionic organotin complex **1** containing redox-active 1,5-Diphenyl-3-(2-pyridyl)formazan ligand was synthesized and is structurally characterized by a single-crystal X-ray diffraction technique. Memory device with sandwich structure Al/Complex **1**/ITO was fabricated using complex **1** as the active layer. The device interestingly demonstrated non-volatile write once read many (WORM) memory behavior, with a high switching on-off ratio of 10^4 and retention time of 4.5×10^4 s. The present work provides a new direction for the development of highly efficient and high-performance write-once-read-many (WORM) type memories based on ionic organotin complexes.